

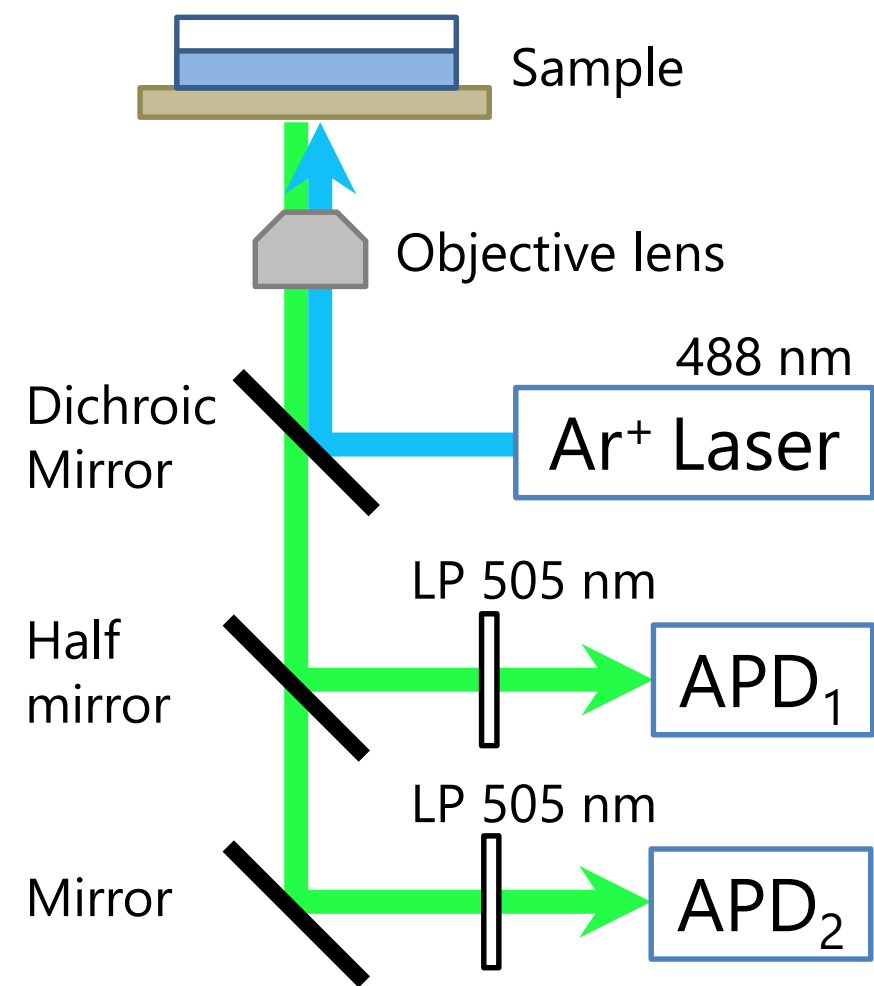


Title	Two-detector number and brightness analysis reveals spatio-temporal oligomerization of proteins in living cells
Author(s)	Fukushima, Ryosuke; Yamamoto, Johtaro; Ishikawa, Hideto; Kinjo, Masataka
Citation	Methods, 140, 161-171 https://doi.org/10.1016/j.ymeth.2018.03.007
Issue Date	2018-05-01
Doc URL	http://hdl.handle.net/2115/73900
Rights	©2018. This manuscript version is made available under the CC-BY-NC-ND 4.0 license http://creativecommons.org/licenses/by-nc-nd/4.0/
Rights(URL)	http://creativecommons.org/licenses/by-nc-nd/4.0/
Type	article (author version)
File Information	METHODS_2017_158.pdf

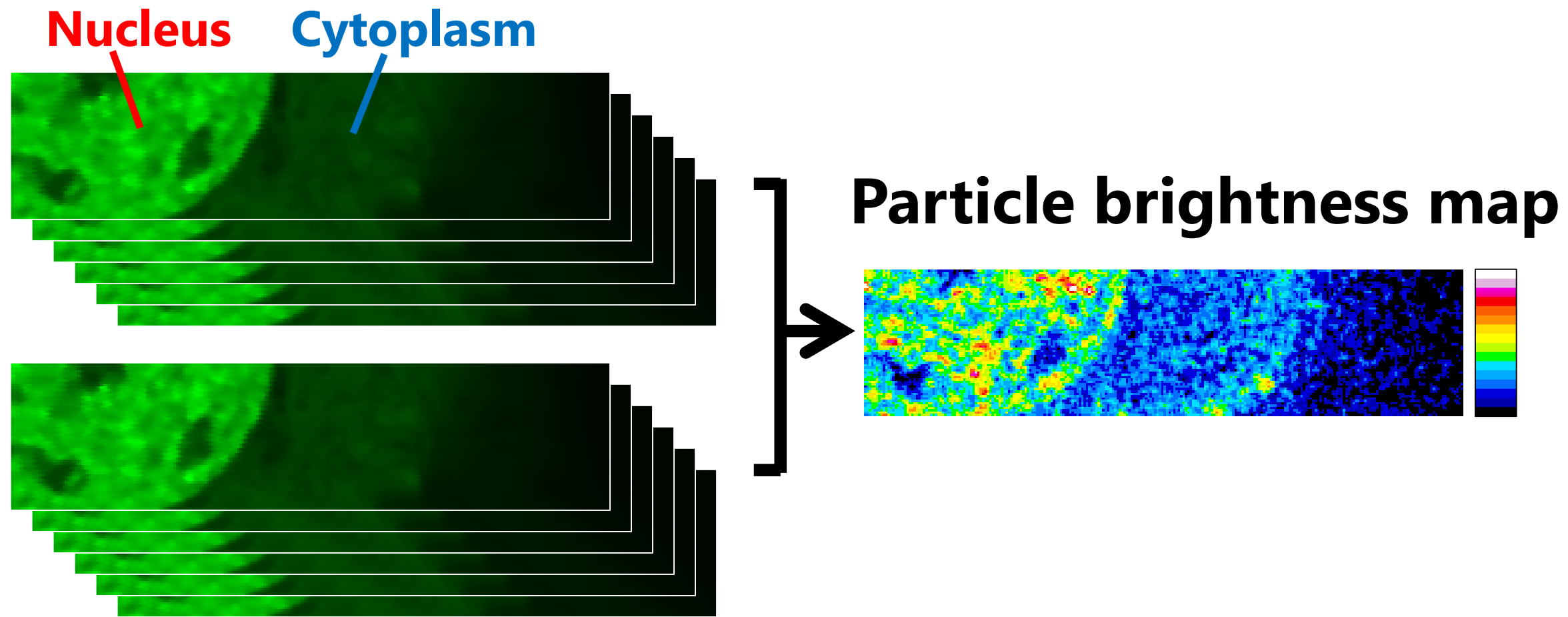


[Instructions for use](#)

Experimental setup



2 stack images of EGFP-GR



Title

Two-Detector Number and Brightness Analysis Reveals Spatio-temporal Oligomerization of Proteins in Living Cells.

Author names and affiliations

Ryosuke Fukushima^a, Johtaro Yamamoto^b, Hideto Ishikawa^a, Masataka Kinjo^{b*}

^aLaboratory of Molecular Cell Dynamics, Graduate School of Life Science, Hokkaido University, Sapporo 001-0021, Japan

^bLaboratory of Molecular Cell Dynamics, Faculty of Advanced Life Science, Hokkaido University, Sapporo 001-0021, Japan

*Corresponding author:

Correspondence should be addressed to M.K. (email: kinjo@sci.hokudai.ac.jp)

Formatting of funding sources

M.K. was partially supported by a grant-in-aid from the Nakatani Foundation for the Advancement of Measuring Technologies in Biomedical Engineering. J.Y. was also partially supported by JSPS KAKENHI (grant number 16K07312).

Highlights (maximum 85 characters, including spaces, per bullet point)

1. We developed a two-detector number and brightness analysis (TD-N&B) system
2. TD-N&B can be used over a wide concentration range
3. TD-N&B detects protein oligomerization and localization in living cells
4. TD-N&B does not require the corrections applied to conventional N&B

Keywords (maximum of 6 keywords)

1. Number and brightness analysis
2. Protein oligomerization
3. Particle brightness
4. Fluorescence imaging
5. Glucocorticoid receptor
6. Dimerization

ABSTRACT (no more than 250 words)

Number and brightness analysis (N&B) is a useful tool for the simultaneous visualization of protein oligomers and their localization, with single-molecule sensitivity. N&B determines particle brightness (fluorescence intensity per particle) and maps the spatial distribution of fluorescently labeled proteins by performing statistical analyses of the image series obtained using laser scanning microscopy. The brightness map reveals presence of the oligomers of the targeted protein and their distribution in living cells. However, even when corrections are applied, conventional N&B is affected by afterpulsing, shot noise, thermal noise, dead time, and overestimation of particle brightness when the concentration of the fluorescent particles changes during measurement.

The drawbacks of conventional N&B can be circumvented by using two detectors, a novel approach that we henceforth call two-detector number and brightness analysis (TD-N&B), and introducing a linear regression of fluorescence intensity. This statistically eliminates the effect of noise from the detectors, and ensures that the correct particle brightness is obtained. Our method was theoretically assessed by numerical simulations and experimentally validated using a dilution series of purified enhanced green fluorescent protein (EGFP), EGFP tandem oligomers in cell lysate, and EGFP tandem oligomers in living cells. Furthermore, this method was used to characterize the complex process of ligand-induced glucocorticoid receptor dimerization and their translocation to the cell nucleus in live cells. Our method can be applied to other oligomer-forming proteins in cell signaling, or to aggregations of proteins such as those that cause neurodegenerative diseases. (239 words)

1. INTRODUCTION

Upon stimulation with specific ligands, many receptors change their localization and oligomeric states. It is, therefore, important to characterize protein localization and oligomerization in live cells.

Fluorescence microscopy coupled with fluorescence fluctuation spectroscopy (FFS) is suitable for monitoring the localization and oligomerization of proteins in living cells. Fluorescence Correlation Spectroscopy (FCS) [1,2], the longest used FFS, can be used to determine the number of particles in the measurement volume, the diffusion coefficient, and the particle brightness (fluorescence intensity per one particle), which can be used to deduce the oligomeric state of the target particles. However, it is difficult to detect long-distance changes in protein localization using FCS because there is usually only one point of measurement. Imaging-based FFS techniques have been

developed to overcome this drawback. They include image correlation spectroscopy (ICS) [3], raster image correlation spectroscopy (RICS) [4,5], temporal image correlation spectroscopy (TICS) [6], and imaging FCS [7]. ICS determines the radius of the particles, the number of particles in a field of view, and the particle brightness. RICS can measure tiny and fast-diffusing particles/molecules, including organic fluorescent dyes, and small proteins. However, the spatial resolution of RICS is always lower than the resolution of the original image, owing to the correlation calculation between adjacent pixels. For example, when we get original images as 512×512 and the correlation is calculated between adjacent 16×16 pixels, the spatial resolution of the result becomes 32×32 . TICS is useful for measuring relatively slow-diffusing particles such as membrane proteins, but is not suitable for fast-diffusing particles because of the low frame rate of confocal imaging. Imaging FCS, which is similar to TICS, uses an electron multiplying charge-coupled device (EMCCD) or a complementary metal oxide semiconductor (CMOS) for image acquisition.

Number and brightness analysis (N&B) is another FFS technique. It produces a map of the number of particles and the particle brightness [8]. Spatial resolution in N&B is the same as that achieved using a laser scanning microscope (LSM). N&B can be applied to fast-diffusing particles, such as diffusing protein in living cells, compared to TICS and Imaging FCS. For TICS and Imaging FCS, frame time (time taken to obtain a frame and lag time of each frame) is important and required to be much shorter than the characteristic decay time of the fluctuating particles (residence time of particles in measurement volume at a pixel) for calculation of correlation in the temporal domain. This restricts their application to measuring slow-diffusing particles, such as membrane proteins. On the other hand, for N&B, frame time is not required to be shorter than the characteristic decay time of the fluctuating particles. However, pixel dwell time (time taken to obtain a pixel value) is required to be much shorter than the characteristic decay time of the fluctuating particles for N&B [8]. N&B does not analyze the temporal intensity fluctuation during crossing of the particles through the measurement volume, but analyze the variance of instantaneous intensity depending on number of particles in measurement volume during shorter time than characteristic decay time (corresponding to diffusion time in FCS). Therefore the lag time of N&B is not effective but only pixel dwell time is effective, and N&B can be applied to relatively fast-diffusing particles such as diffusing protein in living cells. Nevertheless, N&B does not determine the characteristic decay time or diffusion coefficient unlike TICS and Imaging FCS. N&B has been used in several studies, including a distribution analysis of the oligomeric receptor protein ErbB1, before and after stimulation with epidermal growth factor

(EGF) [9]. This study revealed the ligand-independent dimerization of ErbB1 when the density of ErbB1 is sufficiently high and the conversion of ErbB1 into its higher oligomeric state after the stimulation. Another example of the use of N&B is for the investigation of the formation of huntingtin peptide inclusions in degenerative neurological disorders [10]. This study revealed a time-dependent formation of inclusions and a two-step pathway to inclusion formation. Yet another example of the use of N&B is for the investigation of dynamin-2 oligomer formation in HIV-1 infection [11]. This study revealed that the low oligomeric state of dynamin-2 was associated with the HIV envelope protein. N&B is useful for investigating the diffusing particles in living cells and for resolving the particles spatially. Currently, it is impossible to predict when and where oligomers or inclusions will form. N&B enables simultaneous measurements to be carried out over relatively wide fields in living cells. Therefore, it is expected that N&B will be used widely for the study of oligomer or aggregation formation. However, the accuracy of conventional N&B is not adequate and the results are easily affected by sample concentration, necessitating correction for detector dead time [12,13] and correction for noise. Furthermore, conventional N&B overestimates particle brightness when the concentration of the fluorescent particles is changed (Supplementary Note S1) or fluorescence intensity is decreased by photobleaching during measurement [14].

In this study, we developed an improved N&B, called two-detector N&B (TD-N&B), which overcomes the problems associated with conventional N&B without any mathematical corrections. We achieved improvements by eliminating noise effects from detectors, by incorporating a two-detector optical system, and by introducing linear regression to compensate for the change in fluorescence intensity. Furthermore, we demonstrated the feasibility of our method quantitatively by analyzing enhanced green fluorescent protein (EGFP) dilution series, and by investigating EGFP tandem oligomers in cell lysate and living cells. Finally, we monitored the dimerization of EGFP-tagged glucocorticoid receptors (EGFP-GR), as a cell signaling process. The nuclear translocation and dimerization of GR were visualized from a time series of the brightness map of EGFP-GR, which was obtained by TD-N&B. This is the first step towards using quantitative imaging to elucidate dynamic GR mechanisms. Moreover, our method can be applied to other oligomer-forming proteins, or to aggregation of proteins, such as those that cause neurodegenerative diseases, which are difficult to visualize in living cells or whole organisms using biochemical methods and molecular biology.

2. METHODS

2.1. Theory

2.1.1. Two-detector number and brightness analysis (TD-N&B)

The experimental setup of the TD-N&B system is shown in Figure 1A. Two image series were obtained simultaneously using a LSM and two avalanche photodiodes (APDs) operating in the photon counting mode (Figure 1B). We used the APDs to detect fluorescence, but it is also possible to use a detector operating in the analog mode or pseudo-photon counting mode with calibration for image acquisition [15]. The calibration includes: the offset; the S factor, which converts photon counts into digital data, and the read-out variance of the detector. Regardless of the operating mode, the pixel dwell time must be short, compared to the characteristic decay time of the particles in the measurement volume to detect the fluctuation in the number of particles, which is a necessary condition for image acquisition. In our condition, pixel dwell time was 12.61 μs . The characteristic decay time of EGFP monomer in solution measured by FCS was 90 μs . The characteristic decay time of EGFP tandem oligomers in cell lysate and living cells and EGFP-GR in living cells were longer than 90 μs , and the pixel dwell time is 10 times shorter than those. The TD-N&B system analyzes the time sequence of the count rate (photon counts per second), which is corresponding to fluorescence intensity at the same pixel in the two-image series. A schematic diagram of count rate as a function of time at one pixel is shown in Figure 1C. TD-N&B determines the particle brightness and the number of particles at every pixel using a linear component and a fluctuation component of the count rate.

The time series of the count rate at a pixel detected by the two avalanche photodiodes APD₁ and APD₂ are given by:

$$I_1(t) = \varepsilon_1 N(t) + D_1(t), \quad (1)$$

$$I_2(t) = \varepsilon_2 N(t) + D_2(t), \quad (2)$$

where $I_1(t)$ and $I_2(t)$ are the count rates detected by APD₁ and APD₂, respectively,

and ε_1 and ε_2 are the particle brightness values detected by APD₁ and APD₂,

respectively (defined as photon counts detected per second per particle). The ratio of ε_1

to ε_2 depends on the performance of the half mirror and the quantum efficiencies of the APDs. $N(t)$ is the number of particles in the measurement volume (the confocal volume of the LSM). $D_1(t)$ and $D_2(t)$ are the noise from APD₁ and APD₂, respectively.

$I_1(t)$, $I_2(t)$, $N(t)$, $D_1(t)$, and $D_2(t)$ can be separated into two components, linear and fluctuating, as follows (Figure 1C):

$$I_1(t) = I_{l1}(t) + \delta I_1(t), \quad (3)$$

$$I_2(t) = I_{l2}(t) + \delta I_2(t), \quad (4)$$

$$N(t) = N_l(t) + \delta N(t), \quad (5)$$

$$D_1(t) = D_{l1}(t) + \delta D_1(t), \quad (6)$$

$$D_2(t) = D_{l2}(t) + \delta D_2(t). \quad (7)$$

where, subscript l represents the linear component and δ signifies the fluctuations. The linear component with offset can be obtained by the least square method from the time sequence of the pixel of interest. The following equation can be constructed from equations (1–7):

$$\begin{aligned} & \langle (I_1(t) - I_{l1}(t))(I_2(t) - I_{l2}(t)) \rangle \\ &= \langle \delta I_1(t) \delta I_2(t) \rangle \\ &= \langle (\varepsilon_1 \delta N(t) + \delta D_1(t))(\varepsilon_2 \delta N(t) + \delta D_2(t)) \rangle \\ &= \varepsilon_1 \varepsilon_2 \langle \delta N(t)^2 \rangle + \varepsilon_1 \langle \delta N(t) \delta D_2(t) \rangle + \varepsilon_2 \langle \delta N(t) \delta D_1(t) \rangle + \langle \delta D_1(t) \delta D_2(t) \rangle \\ &= \varepsilon_1 \varepsilon_2 \langle \delta N(t)^2 \rangle, \end{aligned} \quad (8)$$

where $\langle \rangle$ represents the ensemble average. Here, we assumed the following:

$$I_{l1}(t) = \varepsilon_1 N_l(t) + D_{l1}(t), \quad (9)$$

$$I_{l2}(t) = \varepsilon_2 N_l(t) + D_{l2}(t). \quad (10)$$

and we can get the following from equations (1–7, 9, 10):

$$\delta I_1(t) = \varepsilon_1 \delta N(t) + \delta D_1(t), \quad (11)$$

$$\delta I_2(t) = \varepsilon_2 \delta N(t) + \delta D_2(t). \quad (12)$$

In addition, we assumed that there is no correlation between the fluctuations of the number of particles and the detector noise ($\langle \delta N(t) \delta D_2(t) \rangle = \langle \delta N(t) \delta D_1(t) \rangle = 0$). There was also no correlation between the fluctuation fractions of the noise from the two different detectors ($\langle \delta D_1(t) \delta D_2(t) \rangle = 0$). Most of the noise effect can be eliminated using those relations.

When the number of particles in the confocal region obeys the Poisson distribution, the variance of the number is equal to the average:

$$\langle N_l(t) \rangle = \langle \delta N(t)^2 \rangle. \quad (13)$$

Finally, the number of particles and the particle brightness can be obtained from equations (8) and (13) as follows:

$$N = \frac{\langle I_1(t) \rangle \langle I_2(t) \rangle}{\langle (I_1(t) - I_{l1}(t)) (I_2(t) - I_{l2}(t)) \rangle}, \quad (14)$$

$$B = \frac{\langle I_{total}(t) \rangle}{N} = \frac{\langle I_{total}(t) \rangle \langle (I_1(t) - I_{l1}(t)) (I_2(t) - I_{l2}(t)) \rangle}{\langle I_1(t) \rangle \langle I_2(t) \rangle}, \quad (15)$$

$$\langle I_{total}(t) \rangle = \langle I_1(t) \rangle + \langle I_2(t) \rangle = \varepsilon \langle N(t) \rangle + \langle D(t) \rangle. \quad (16)$$

where $I_{total}(t) = I_1(t) + I_2(t)$, $\varepsilon = \varepsilon_1 + \varepsilon_2$, and $D(t) = D_1(t) + D_2(t)$. When the count rate is markedly larger than the noise intensity, we can assume the following:

$$\langle I_1(t) \rangle \approx \varepsilon_1 \langle N(t) \rangle, \quad (17)$$

$$\langle I_2(t) \rangle \approx \varepsilon_2 \langle N(t) \rangle, \quad (18)$$

$$\langle I_{total}(t) \rangle = \langle I_1(t) \rangle + \langle I_2(t) \rangle \approx \varepsilon \langle N(t) \rangle. \quad (19)$$

This theory can be applied to even non-linear concentration change when the concentration change is much slower than frame time, and the concentration change in a small sliding segment (described in the Analysis condition section) can be assumed as linear.

If there are only monomers and dimers of fluorescently labeled target particles, the ratio between the two can be analyzed using an advanced approach. The count rate arising from a monomer and dimer is given by:

$$I = \varepsilon_m N_m + \varepsilon_d N_d, \quad (20)$$

where I is the count rate, ε_m and ε_d are the particle brightness values of the monomer and dimer, respectively, which must be determined or measured by reference measurement, and N_m and N_d are the numbers of monomers and dimers, respectively. The ratio of the number of monomers to the number of dimers is given by:

$$\frac{N_d}{N_m} = \frac{1 - \frac{B}{\varepsilon_m}}{\frac{\varepsilon_d}{\varepsilon_m} \left(\frac{B}{\varepsilon_m} - \frac{\varepsilon_d}{\varepsilon_m} \right)}, \quad (21)$$

where B/ε_m is the particle brightness normalized to the particle brightness of an EGFP monomer. $\varepsilon_d/\varepsilon_m$ is the ratio between the particle brightness of the monomer and that of the dimer when the measurements are performed independently.

2.1.2. Simulation

The fluctuating count rate was numerically simulated using MATLAB R2009b (MathWorks, USA), and the simulated results from conventional N&B and TD-N&B were compared. In the simulation, the particle brightness and the average number of particles were $\varepsilon = 4$ [kHz] and $\langle N(t) \rangle = 50$, respectively. The linear component

$N_I(t)$ was calculated using the given slope and $\langle N(t) \rangle$, and the fluctuation component $\delta N(t)$ was generated from a random number obeying the Poisson distribution. Finally, the total count rate $I_{total}(t)$ was calculated using equation (19), and it was distributed among $I_1(t)$ and $I_2(t)$ in a 2:3 ratio.

2.2. Materials

2.2.1. Purification of EGFP

EGFP was purified using the his-tag method, which was described previously [16].

2.2.2. Preparation of EGFP tandem oligomer lysate

COS-7 cells were maintained at 37°C under a humidified atmosphere of 5% CO₂, in Dulbecco's modified Eagle's medium (DMEM; #D5796; Sigma-Aldrich, USA) supplemented with 10% fetal bovine serum (FBS; GE Healthcare, USA), 100 µg/mL penicillin G (Sigma-Aldrich, USA), and 100 µg/mL streptomycin (Sigma-Aldrich, USA). The COS-7 cells were seeded into a 6-well chamber (#140675, Thermo Fisher Scientific, USA) and incubated for 24 h. The cells (5×10^5 cells) were transfected with 1.0 µg of EGFP-C1 plasmids encoding EGFP monomer, or the plasmids encoding flexible linker (FL)-linked EGFP tandem oligomers (2–5 mer) [16] using Lipofectamine 2000 (Life Technologies, USA). The cells were incubated for 24 h. The medium was then renewed, followed by a 24-h incubation. The cells were then lysed using CellLytic M cell lysis reagent (Sigma-Aldrich, USA), and a protease inhibitor cocktail (Sigma-Aldrich, USA). The cell debris was then scraped, collected into microtubes, and centrifuged at 20,400 g for 10 min at 4°C. The supernatant cell lysate was collected and subjected to further analysis.

2.2.3. Preparation of EGFP tandem oligomer-transfected U2OS cells

U2OS cells were maintained at 37°C under a humidified atmosphere of 5% CO₂ in McCoy's 5A medium (#16600-820; Life Technologies, USA) supplemented with 10% charcoal-stripped fetal bovine serum (CS-FBS; Thermo Fisher Scientific, USA), 100 µg/mL penicillin G (Sigma-Aldrich, USA), and 100 µg/mL streptomycin (Sigma-Aldrich, USA). The U2OS cells were seeded into an 8-well chambered coverglass (#155411, Thermo Fisher Scientific, USA) and incubated for 24 h. The cells (1.6×10^4 cells) were then transfected with 0.1 µg of EGFP-C1 plasmids encoding EGFP monomer, or the plasmids encoding FL-linked EGFP tandem oligomers (2–5

mer) [16] using ViaFect (Promega, USA). The cells were incubated for 24 h. The medium was then renewed and incubation was continued for 24 h. The medium was renewed again before the measurements were taken.

2.2.4. Measurement of EGFP-GR translocation

U2OS cells were seeded into an 8-well chamber cover glass (Thermo Fisher Scientific, USA), and incubated at 37°C in 5% CO₂ for 24 h. The cells (1.6×10^4 cells) were transfected with 0.1 µg of EGFP-GR^{WT} and EGFP-GR^{A458T} plasmids using ViaFect (Promega, USA). The cells were incubated for 24 h. The medium was then renewed and incubation was continued for 24 h. The medium was renewed again before the measurements were taken. The measurements were performed immediately after the addition of dexamethasone (final concentration of 100 nM).

2.2.5. Image acquisition for TD-N&B

Confocal fluorescence microscopy images were obtained using an LSM 710 META ConfoCor3 system (Carl Zeiss, Germany) with a C-Apochromat 40×/1.2W Corr objective (Carl Zeiss). The EGFP was excited at a wavelength of 488 nm. EGFP fluorescence was split into two channels by a half mirror, and filtered using a long-pass filter (LP505). The pinhole size was 34 µm. The zoom factor was × 6. The X- and Y-scanning sizes were 256 × 64 pixels. The pixel dwell time was 12.61 µs. Scanning was bi-directional. Except for in the GR experiment, 1,000 images were sequentially obtained; 10,000 images were obtained in the GR experiment. The laser had an output of 0.25 µW at the objective for all measurements.

2.2.6. FCS measurements

FCS measurements were performed using an LSM 710 META ConfoCor3 system (Carl Zeiss) with a C-Apochromat 40×/1.2W Corr objective (Carl Zeiss). The EGFP was excited at a wavelength of 488 nm. EGFP fluorescence was split into two channels by a half mirror and filtered using a long-pass filter (LP505). The pinhole size was 32 µm. The measurement duration was 10 s × 10 times. A multi-component diffusion model with one triplet state was used for curve-fitting:

$$G(\tau) = 1 + \left[1 + \frac{T}{1-T} \exp\left(-\frac{\tau}{\tau_{triplet}}\right) \right] \frac{1}{N} \left[\sum_i^m F_i \left(1 + \frac{\tau}{\tau_i}\right)^{-1} \left(1 + \frac{\tau}{s^2 \tau_i}\right)^{-\frac{1}{2}} \right], \quad (22)$$

where, $G(\tau)$ is a temporal autocorrelation function, T is the triplet fraction, $\tau_{triplet}$ is the relaxation time of the triplet state, N is the average number of fluorescent particles in the measurement volume, F_i and τ_i are the fraction and diffusion time of the i th component, respectively, s is a structure parameter representing the ratio of the beam waist to the axial radius, and m is the number of components. For the purified EGFP experiment, $m = 1$; for the lysate and live cell experiments, $m = 2$. After pinhole adjustment, the structure parameter was determined using a 10^{-7} M standard solution of rhodamine 6G for which the diffusion coefficient is known as $D_{Rh6G} = 414 \mu\text{m}^2/\text{s}$ [17,18].

Particle brightness was calculated as count rate divided by the number of particles, determined by FCS. In the lysate, high-intensity fluorescence bursts were occasionally observed. This might be caused by sporadic passage of aggregated EGFP tandem oligomers. The particle brightness is not significantly affected by this because the aggregates are rarely formed (Supplementary Figure S2).

2.2.7. Analysis conditions

Boxcar filtering [19] and median filtering [8] were introduced for TD-N&B. Except for the GR experiments, 1,000 images were obtained and divided into small sliding segments. The length of each sliding segment was determined to be 200, and there were 801 sliding segments. The TD-N&B calculation was performed on every sliding segment. It produced 801 maps for particle brightness and 801 maps showing number of particles. Median filtering was applied to these two maps. For each pixel, the first-neighbor pixels (3×3) were analyzed. The pixel value was replaced by the median value of the 3×3 array. After median filtering, the results for the two maps were obtained by averaging the 801 maps.

For the GR experiments, 10,000 images were divided into medium sliding segments. We determined the length of each medium sliding segment to be 1,000. This produced 9,001 medium sliding segments. An averaged particle brightness map and an averaged number of particles map were calculated for every medium sliding segment, as described above. Finally, 9,001 maps of the particle brightness and the number of particles were obtained. To reduce the enormous computation time required, parallel computing with a graphics processing unit (GPU) was performed using a JETSON TK-1 developer kit (NVIDIA, USA). The calculation time was approximately 6 h for 10,000 images.

The length of each sliding segment needs to be determined for TD-N&B analysis.

Longer sliding segments produce more accurate maps, although there is the possibility that artifacts may arise owing to nonlinear changes in count rate, which are caused by cell migration or photobleaching. However, shorter sliding segments produce less accurate maps. Monomers and oligomers cannot be distinguished in the maps if the sliding segments are too short.

After the calculation, the average count rate and average particle brightness of a map was obtained in the region of interest (ROI). For the purified EGFP experiments, the ROI was set at 254×62 because the pixels at the edges of the images were distorted by median filtering. For the lysate experiments, the ROI was set at 254×62 , and the average particle brightness was calculated by fitting the histogram of particle brightness into the Gaussian distribution in order to avoid the distortion caused by aggregated EGFP tandem oligomers. For the cell experiments, the ROI was set in the nucleus or in the cytoplasm along the nuclear envelope.

3. RESULTS

3.1. Comparison by simulation

Conventional N&B assumes that the fluorescence intensity is ergodic and its properties can therefore be deduced from a single, sufficiently long, random sample of the process. However, fluorescence intensity can change during the measurement, owing to changes in concentration or to photobleaching, especially in living cells. Therefore, the results of conventional N&B can be seriously distorted. A simulation was performed to assess these effects. In the simulation, ε was fixed at 4 kHz and $\langle N(t) \rangle$ was fixed at 50. As a model, it was assumed that the count rate was detected by APD₁ and APD₂ in a 3:2 ratio, and the slope of the count rate depended on the change in the concentration of the fluorophore. The simulation results are shown in Figure 2. Typical simulated signals with a slope of 0 and signals with linear concentration change with a slope of 0.1 are shown in A and B (Figure 2), respectively. The average particle brightness in conventional N&B increased with the slope of the count rate change (Figure 2CC). The average number of particles in conventional N&B decreased with the count rate change (Figure 2D). The results suggest that conventional N&B is not suitable as a quantitative method when the count rate is not stable (slope $\neq 0$). Introducing a linear regression of the TD-N&B signals eliminated the effect of concentration change, and the average particle brightness and the average number of particles remained constant.

3.2. TD-N&B in solution

Figure 3 illustrates the dependency of particle brightness and the number of particles on the concentration of EGFP, measured by conventional N&B and TD-N&B. The samples were taken from a series comprising various dilutions of EGFP in phosphate-buffered saline. The average count rate increased with the concentration of EGFP (Figure 3A). Theoretically, the average number of particles increases with concentration, but average particle brightness remains constant. In the present study, the average particle brightness decreased at concentrations over 0.05 μM , as determined by conventional N&B (Figure 3B). The average number of particles did not increase with concentration (Figure 3C). In contrast, the average particle brightness was correctly estimated, even at concentrations over 0.05 μM , and the average number of particles increased with concentration when TD-N&B was used. This suggests that the quantitative results for particle brightness and the number of particles determined by TD-N&B are more accurate than those determined by conventional N&B. However, average particle brightness was not constant at concentrations under 0.05 μM when either method was used. This was caused by insufficient photon counts for statistical analyses.

3.3. *In vitro* investigation of EGFP tandem oligomers using TD-N&B

Next, we confirmed the dependency of particle brightness on the number of EGFP units. The particle brightness of EGFP does not precisely correspond to the number of EGFP units, because it is possible that particle brightness is affected by molecular mechanisms such as energy transfer and/or quenching. Therefore, TD-N&B requires control and calibration experiments. Those experiments were performed on EGFP tandem oligomers in the cell lysate. The schematic sequences of the EGFP tandem oligomers are shown in Figure 4A. Particle brightness was measured using both TD-N&B and conventional N&B, and the results were also compared with those of experiments that used FCS as a control method (Figure 4B). Each average particle brightness was normalized to the average particle brightness of the EGFP monomers. Significant differences in normalized particle brightness using FCS, TD-N&B, and conventional N&B are shown in Figure 4C–E. A comparison between 3 different methods is shown in Figure 4F. With FCS, the normalized particle brightness increased with the number of EGFP units. Similar results were obtained using TD-N&B, but different results were obtained using conventional N&B. This was probably due to underestimation of particle brightness using conventional N&B. Particle brightness versus count rate plot is shown in supplementary figure S3A.

3.4. Investigation of EGFP tandem oligomers in live cells

Figures 5A–O show the count rate, the particle brightness, and the number of EGFP tandem oligomers in living cells. Normalized particle brightness was compared using FCS and TD-N&B, as seen in Figures 5P and 5Q. Significant differences in normalized particle brightness in the nucleus and cytoplasm, as determined by FCS, are shown in Figures 5R and 5S. Significant differences in normalized particle brightness in the nucleus and cytoplasm, as determined by TD-N&B are shown in Figures 5T and 5U. The results obtained using TD-N&B were similar to those obtained using FCS. Normalized particle brightness increased linearly in the cytoplasm. However, the average values of normalized particle brightness did not correspond with the number of EGFP units in the cytoplasm, unlike in the lysate, indicating that some of the EGFP units in the EGFP tandem oligomers did not fluoresce, owing to the effects of quenching, temperature, pH, and photobleaching. A detailed investigation of this phenomenon in the near future is warranted.

Moreover, normalized particle brightness did not increase linearly in the nucleus (Figures 5P and 5Q). One explanation is that larger EGFP tandem oligomers do not pass through the nuclear pores easily, resulting in a nuclear count rate that is too low to be determined accurately. Another explanation is that some of the EGFP tandem oligomers are digested into smaller fragments, which pass through the nuclear pores. The particle brightness versus count rate plot is shown in supplementary figure S3B and S3C.

3.5. GR measurement

Finally, we investigated the spatio-temporal distribution of nuclear translocating GR using TD-N&B. GRs are nuclear receptors that are ubiquitously expressed in almost all cells in the human body. GRs and their associated steroid ligands, the glucocorticoid hormones, regulate numerous genes that modulate the immune system [20], and play a critical role in the development and the constitutive activity of the central nervous system [21]. Although steroid hormones were first used in clinical treatments in 1948 [20], the detailed molecular mechanism of GR action remains unclear. This lack of basic mechanistic understanding hampers our ability to efficiently treat/avoid the serious side-effects related to prolonged treatment with steroid hormones.

GRs act as transcription factors by binding to the glucocorticoid response elements (GREs) in the nucleus, and act as modulators of other transcription factors. They exhibit complex dynamic behaviors such as nuclear translocation upon stimulation with steroid hormones and assembly at the DNA as dimers [22–24]. However, whether GRs form

monomers or dimers during translocation is still unknown.

Figure 6 shows the particle brightness of EGFP-GR^{WT} and EGFP-GR^{A458T} in U2OS cells during nuclear translocation, as determined by TD-N&B. GR^{A458T} is a dimerization-deficient mutant. The average count rate and average particle brightness were calculated among pixels in a selected ROI. Average particle brightness was normalized to the average particle brightness of the EGFP monomer. Therefore, a normalized particle brightness of 1.0 or 2.0 indicated EGFP-GR monomers and dimers, respectively. The average count rate of both the wild-type (WT) and A458T increased in the nucleus and decreased in the cytoplasm, owing to nuclear translocation. The normalized particle brightness of both the WT and A458T was constant at approximately 1.0 in the cytoplasm, indicating that EGFP-GR^{WT} and EGFP-GR^{A458T} were monomeric. However, the normalized particle brightness of EGFP-GR^{WT} increased in the nucleus to 1.63 (Figure 6F), compared to the case in A458T, in which the normalized particle brightness increased to 1.34 (Figure 6H). The increase in the normalized particle brightness in the nucleus after translocation was larger in the EGFP-GR^{WT} than in EGFP-GR^{A458T}. This implies that EGFP-GR^{WT} translocated as a monomer and dimerized in the nucleus.

4. DISCUSSION

We have developed and present here a two-detector optical system significantly improved N&B analysis, which we call TD-N&B. TD-N&B enables a more precise quantitative determination of particle brightness and the number of particles, compared to conventional N&B. Underestimation of particle brightness by conventional N&B in regions of high concentration was observed (Figure 3B), which is caused by the effect of dead time in the APDs. The authors of previous studies [12,13] have described a correction method for such an effect. However, TD-N&B provides accurate measurements without the need for detector dead time correction. Furthermore, TD-N&B and the linear regression analysis developed here can also eliminate other noise, including afterpulsing, shot noise, and thermal noise from detectors. Generally, it is difficult to completely predict such noise and correct the fluorescence intensity accordingly. Therefore, TD-N&B has a marked advantage in this respect. TD-N&B is applicable to concentration change during measurement in time regimes where changes in fluorescence intensity can be assumed to be linear (Figure 2). The sensitivity to increased particle brightness using EGFP tandem oligomers is clearly demonstrated in Figure 4. The normalized particle brightness of TD-N&B corresponds

to the number of EGFP units in the lysate experiment. This suggests that the number of EGFP units included in the EGFP tandem oligomers can be estimated by normalized particle brightness. We also performed TD-N&B analysis in live cells (Figure 5). The normalized particle brightness in TD-N&B increased linearly with the number of EGFP units in the live cells, but it did not directly correspond to the number of EGFP units. This suggests that the number of EGFP units included in the EGFP tandem oligomers needs to be estimated carefully. However, we were able to deduce oligomer formation from the increasing normalized particle brightness.

Finally, we were able to simultaneously monitor protein behaviors, such as the nuclear translocation and dimerization of GR in living cells using TD-N&B. It is impossible to investigate the translocation of GR using conventional N&B, because the count rate in a ROI is dramatically changed by nuclear translocation. After translocation, the normalized particle brightness of EGFP-GR^{WT} was 1.63, and the normalized particle brightness of EGFP-GR^{A458T} was 1.34. When we assumed that the normalized particle brightness of EGFP-GR was 2.0, as it should ideally be when EGFP-GR is dimerized, the concentration ratio of the number of monomers to dimers of EGFP-GR^{WT} was estimated to be 1:0.85, and the concentration ratio of EGFP-GR^{A458T} was 1:0.26, according to equation (21). However, the normalized particle brightness of the EGFP dimers was actually 1.65 times higher than that of the EGFP monomers. Therefore, because the normalized particle brightness of EGFP-GR was 1.65 and not 2.0 when EGFP-GR was dimerized, the concentration ratio between the monomers and dimers of EGFP-GR^{WT} was 1:19.1, and the concentration ratio between the monomers and dimers of EGFP-GR^{A458T} was 1:0.66. Hence, it is possible to estimate the ratio of monomers to dimers in living cells using TD-N&B.

Our results suggest that a small amount of EGFP-GR^{A458T} dimerized in the nucleus. It has been reported that GR^{A458T} is partially dimerized in the nucleus [25]. Moreover, it has also been reported that GR dimerizes in the cytoplasm when its concentration is high [26]. The concentration of GR may have been low in our experiments, compared to the case in previous reports.

5. CONCLUSIONS

We have developed TD-N&B from N&B. The problems of conventional N&B were solved by introducing a two-detector optical system and linear regression of fluorescence intensity. The accuracy of TD-N&B was confirmed quantitatively by simulations and measurements in a dilution series of purified EGFP, EGFP tandem oligomers in cell lysate and living cells. TD-N&B can sequentially detect protein

oligomerization over a wide field, even if the protein is diffused in living cells. Finally, the spatio-temporal measurement of localization and oligomer state change was demonstrated by an investigation of GR. We expect that TD-N&B will be useful for the discovery of compounds that promote/inhibit oligomerization, especially those that inhibit aggregation, which may be useful for the treatment of neurodegenerative diseases.

Figure 1. The concept of two-detector number and brightness analysis (TD-N&B).

(A) Schematic diagram of the experimental setup. (B) Cartoons of image series simultaneously obtained by two avalanche photodiodes (APD). (C) Linear regression of count rate. Count rate at the same pixel was plotted as a function of time.

Figure 2. Two-detector number and brightness analysis (TD-N&B) and conventional N&B simulation over a range of concentrations.

Numerical simulation in a comparison between TD-N&B and conventional N&B.

$\varepsilon = 4$ [kHz] and $\langle N(t) \rangle = 50$. The count rate was distributed in a 3:2 ratio between APD₁ and APD₂ by a half mirror. A linear concentration change was assumed, and it caused a linear change of count rate. (A) Simulated count rate with a slope of 0. (B) Simulated count rate with a linear concentration change with a slope of 0.1. (C) Average particle brightness as a function of the slope. (D) Average number of particles as a function of the slope.

Figure 3. Two-detector number and brightness analysis (TD-N&B) and conventional N&B experiments on a purified EGFP diluted series.

Dependency of particle brightness and the number of particles on the concentration of EGFP. The experiment was performed with a series of purified EGFP dilutions. The concentrations were measured by fluorescence correlation spectroscopy (FCS). (A) Average count rate versus concentration. (B) Average particle brightness versus concentration. (C) Average number of particles versus concentration.

Figure 4. Two-detector number and brightness analysis (TD-N&B), fluorescence correlation spectroscopy (FCS), and conventional N&B experiments on EGFP tandem oligomers *in vitro*.

The particle brightness of EGFP tandem oligomers in lysates was investigated using FCS, TD-N&B, and conventional N&B. Average particle brightness was normalized to

that of EGFP monomers. (A) Schematic structure of EGFP tandem oligomers. (B) Comparison of normalized particle brightness among the different methods (N = 5). (C–E) Significant differences in normalized particle brightness as determined by FCS, TD-N&B, and conventional N&B (ns: not significant; *p < 0.05, **p < 0.01). (F) Significant differences in normalized particle brightness among FCS, TD-N&B, and conventional N&B (ns: not significant; *p < 0.05, **p < 0.01).

Figure 5. Two-detector number and brightness analysis (TD-N&B) and FCS experiments on EGFP tandem oligomers *in vivo*.

Count rate, particle brightness, and the number of particles of EGFP tandem oligomers in living cells. Count rate images (A–E), particle brightness images (F–J), and the number of particles images (K–O). N: nucleus; C: cytoplasm. (P) Comparison of normalized particle brightness determined by FCS (N = 5). Nuc: in the nucleus; Cyto: in the cytoplasm. (Q) Comparison of normalized particle brightness determined by TD-N&B (N = 5). (R–U) Significant differences in normalized particle brightness in the nucleus and cytoplasm as determined by FCS and TD-N&B (ns: not significant; *p < 0.05, **p < 0.01).

Figure 6. Particle brightness of EGFP-GR^{WT} and EGFP-GR^{A458T} during nuclear translocation.

GR^{A458T} is a dimerization-deficient mutant. U2OS cells were transfected with EGFP-GR^{WT} and EGFP-GR^{A458T}, and stimulated with 100 nM dexamethasone. (A, B) Count rate image of EGFP-GR^{WT} before and after translocation. N: nucleus; C: cytoplasm. (C, D) Particle brightness image of EGFP-GR^{WT} before and after translocation. Average count rate during the translocation of EGFP-GR^{WT} (E) and EGFP-GR^{A458T} (G). Normalized particle brightness during the translocation of EGFP-GR^{WT} (F) and EGFP-GR^{A458T} (H).

6. REFERENCES

- [1] E.L. Elson, D. Magde, Fluorescence correlation spectroscopy. I. Conceptual basis and theory, *Biopolymers*. 13 (1974) 1–27. doi:10.1002/bip.1974.360130102.
- [2] D. Magde, E.L. Elson, W.W. Webb, Fluorescence correlation spectroscopy. II. An experimental realization, *Biopolymers*. 13 (1974) 29–61. doi:10.1002/bip.1974.360130103.
- [3] N.O. Petersen, P.L. Höddelius, P.W. Wiseman, O. Seger, K.E. Magnusson, Quantitation of

- membrane receptor distributions by image correlation spectroscopy: concept and application, *Biophys. J.* 65 (1993) 1135–1146. doi:10.1016/S0006-3495(93)81173-1.
- [4] M.A. Digman, P. Sengupta, P.W. Wiseman, C.M. Brown, A.R. Horwitz, E. Gratton, Fluctuation Correlation Spectroscopy with a Laser-Scanning Microscope: Exploiting the Hidden Time Structure, *Biophys. J.* 88 (2005) L33–L36. doi:10.1529/biophysj.105.061788.
- [5] M.A. Digman, C.M. Brown, P. Sengupta, P.W. Wiseman, A.R. Horwitz, E. Gratton, Measuring Fast Dynamics in Solutions and Cells with a Laser Scanning Microscope, *Biophys. J.* 89 (2005) 1317–1327. doi:10.1529/biophysj.105.062836.
- [6] P.W. Wiseman, J.A. Squier, M.H. Ellisman, K.R. Wilson, Two-photon image correlation spectroscopy and image cross-correlation spectroscopy, *J. Microsc.* 200 (2000) 14–25. doi:10.1046/j.1365-2818.2000.00736.x.
- [7] B. Kannan, J.Y. Har, P. Liu, I. Maruyama, J.L. Ding, T. Wohland, Electron Multiplying Charge-Coupled Device Camera Based Fluorescence Correlation Spectroscopy, *Anal. Chem.* 78 (2006) 3444–3451. doi:10.1021/ac0600959.
- [8] M.A. Digman, R. Dalal, A.F. Horwitz, E. Gratton, Mapping the Number of Molecules and Brightness in the Laser Scanning Microscope, *Biophys. J.* 94 (2008) 2320–2332. doi:10.1529/biophysj.107.114645.
- [9] P. Nagy, J. Claus, T.M. Jovin, D.J. Arndt-Jovin, Distribution of resting and ligand-bound ErbB1 and ErbB2 receptor tyrosine kinases in living cells using number and brightness analysis, *Proc. Natl. Acad. Sci.* 107 (2010) 16524–16529. doi:10.1073/pnas.1002642107.
- [10] G. Ossato, M.A. Digman, C. Aiken, T. Lukacsovich, J.L. Marsh, E. Gratton, A Two-Step Path to Inclusion Formation of Huntingtin Peptides Revealed by Number and Brightness Analysis, *Biophys. J.* 98 (2010) 3078–3085. doi:10.1016/j.bpj.2010.02.058.
- [11] D.M. Jones, L.A. Alvarez, R. Nolan, M. Ferriz, R. Sainz Urruela, X. Massana-Muñoz, H. Novak-Kotzer, M.L. Dustin, S. Padilla-Parra, Dynamin-2 Stabilizes the HIV-1 Fusion Pore with a Low Oligomeric State, *Cell Rep.* 18 (2017) 443–453. doi:10.1016/j.celrep.2016.12.032.
- [12] J. Hendrix, W. Schrimpf, M. Höller, D.C. Lamb, Pulsed Interleaved Excitation Fluctuation Imaging, *Biophys. J.* 105 (2013) 848–861. doi:10.1016/j.bpj.2013.05.059.
- [13] L.N. Hillesheim, J.D. Müller, The Photon Counting Histogram in Fluorescence Fluctuation Spectroscopy with Non-Ideal Photodetectors, *Biophys. J.* 85 (2003) 1948–1958. doi:10.1016/S0006-3495(03)74622-0.
- [14] K.-H. Hur, P.J. Macdonald, S. Berk, C.I. Angert, Y. Chen, J.D. Mueller, Quantitative Measurement of Brightness from Living Cells in the Presence of Photodepletion, *PLoS One.* 9 (2014) e97440. doi:10.1371/journal.pone.0097440.
- [15] R.B. Dalal, M.A. Digman, A.F. Horwitz, V. Vetri, E. Gratton, Determination of particle number and brightness using a laser scanning confocal microscope operating in the analog mode, *Microsc.*

- Res. Tech. 71 (2008) 69–81. doi:10.1002/jemt.20526.
- [16] M. Oura, J. Yamamoto, H. Ishikawa, S. Mikuni, R. Fukushima, M. Kinjo, Polarization-dependent fluorescence correlation spectroscopy for studying structural properties of proteins in living cell, *Sci. Rep.* 6 (2016) 31091. doi:10.1038/srep31091.
- [17] C.B. Müller, A. Loman, V. Pacheco, F. Koberling, D. Willbold, W. Richtering, J. Enderlein, Precise measurement of diffusion by multi-color dual-focus fluorescence correlation spectroscopy, *Europhys. Lett.* 83 (2008) 46001. doi:10.1209/0295-5075/83/46001.
- [18] C.T. Culbertson, S.C. Jacobson, J. Michael Ramsey, Diffusion coefficient measurements in microfluidic devices., *Talanta.* 56 (2002) 365–73. doi:10.1016/S0039-9140(01)00602-6.
- [19] A. Trullo, V. Corti, E. Arza, V.R. Caiolfa, M. Zamai, Application limits and data correction in number of molecules and brightness analysis, *Microsc. Res. Tech.* 76 (2013) 1135–1146. doi:10.1002/jemt.22277.
- [20] D.W. Cain, J.A. Cidlowski, Immune regulation by glucocorticoids, *Nat. Rev. Immunol.* 17 (2017) 233–247. doi:10.1038/nri.2017.1.
- [21] M. Srinivasan, D.K. Lahiri, Glucocorticoid-Induced Leucine Zipper in Central Nervous System Health and Disease, *Mol. Neurobiol.* 54 (2017) 8063–8070. doi:10.1007/s12035-016-0277-5.
- [22] S. Oasa, A. Sasaki, J. Yamamoto, S. Mikuni, M. Kinjo, Homodimerization of glucocorticoid receptor from single cells investigated using fluorescence correlation spectroscopy and microwells, *FEBS Lett.* 589 (2015) 2171–2178. doi:10.1016/j.febslet.2015.07.003.
- [23] M. Tiwari, S. Oasa, J. Yamamoto, S. Mikuni, M. Kinjo, A Quantitative Study of Internal and External Interactions of Homodimeric Glucocorticoid Receptor Using Fluorescence Cross-Correlation Spectroscopy in a Live Cell, *Sci. Rep.* 7 (2017) 4336. doi:10.1038/s41598-017-04499-7.
- [24] B.F. Luisi, W.X. Xu, Z. Otwinowski, L.P. Freedman, K.R. Yamamoto, P.B. Sigler, Crystallographic analysis of the interaction of the glucocorticoid receptor with DNA, *Nature.* 352 (1991) 497–505. doi:10.1038/352497a0.
- [25] C.M. Jewell, A.B. Scoltock, B.L. Hamel, M.R. Yudt, J.A. Cidlowski, Complex Human Glucocorticoid Receptor dim Mutations Define Glucocorticoid Induced Apoptotic Resistance in Bone Cells, *Mol. Endocrinol.* 26 (2012) 244–256. doi:10.1210/me.2011-1116.
- [26] S. Robertson, J.M. Rohwer, J.P. Hapgood, A. Louw, Impact of Glucocorticoid Receptor Density on Ligand-Independent Dimerization, Cooperative Ligand-Binding and Basal Priming of Transactivation: A Cell Culture Model, *PLoS One.* 8 (2013) e64831. doi:10.1371/journal.pone.0064831.

Supplementary Note S1

We will show that the concentration change of fluorescent particles in measurement time causes overestimation of particle brightness when the linear regression is not performed. We assume linear concentration change in measurement time for simplification. Let T be the number of frames. $N(t)$ can be separated into two components, linear and fluctuating:

$$N(t) = N_l(t) + \delta N(t). \quad (\text{S1})$$

We assume that the linear component has a slope of A and an offset of B as the following:

$$N_l(t) = At + B. \quad (\text{S2})$$

In addition, time average corresponds to the time average of linear component:

$$\langle N(t) \rangle = \langle N_l(t) \rangle. \quad (\text{S3})$$

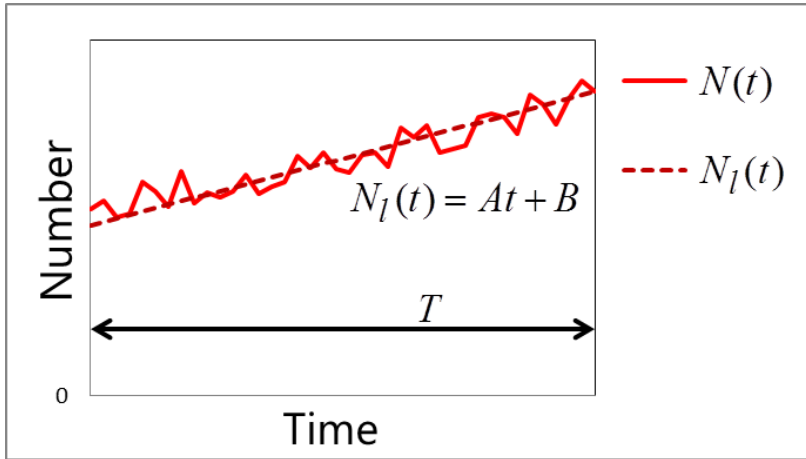


Figure 1. Linear concentration change in measurement time.

Number of particle as a function of time. Solid red line is the number of particles. Dotted line is linear component of $N(t)$.

Apparent number of particles N_{app} and apparent particle brightness B_{app} without linear regression are defined as follows:

$$N_{app} = \frac{\langle I_1(t) \rangle \langle I_2(t) \rangle}{\langle (I_1(t) - \langle I_1(t) \rangle)(I_2(t) - \langle I_2(t) \rangle) \rangle}, \quad (\text{S4})$$

$$B_{app} = \frac{\langle I_{total}(t) \rangle}{N_{app}}. \quad (\text{S5})$$

Substitution of equation (1, 2) and (S1, S3) into the following equation gives

$$\begin{aligned} & \langle (I_1(t) - \langle I_1(t) \rangle)(I_2(t) - \langle I_2(t) \rangle) \rangle \\ &= \varepsilon_1 \varepsilon_2 \langle (N(t) - \langle N(t) \rangle)^2 \rangle \\ &= \varepsilon_1 \varepsilon_2 \langle (N_I(t) + \delta N(t) - \langle N(t) \rangle)^2 \rangle \\ &= \varepsilon_1 \varepsilon_2 \left\{ \langle (N_I(t) - \langle N_I(t) \rangle)^2 \rangle + 2 \langle (N_I(t) - \langle N(t) \rangle) \delta N(t) \rangle + \langle \delta N(t)^2 \rangle \right\} \\ &= \varepsilon_1 \varepsilon_2 \left\{ \langle (N_I(t) - \langle N_I(t) \rangle)^2 \rangle + \langle \delta N(t)^2 \rangle \right\}. \end{aligned} \quad (\text{S6})$$

Here, we assumed the following:

$$\langle (N_I(t) - \langle N(t) \rangle) \delta N(t) \rangle = 0. \quad (\text{S7})$$

$\langle N_I(t) \rangle$ and $\langle (N_I(t) - \langle N_I(t) \rangle)^2 \rangle$ are calculated as follows:

$$\begin{aligned} \langle N_I(t) \rangle &= \frac{1}{T} \int_0^T At + B dt \\ &= \frac{1}{2} AT + B, \end{aligned} \quad (\text{S8})$$

$$\begin{aligned} \langle (N_I(t) - \langle N_I(t) \rangle)^2 \rangle &= \frac{1}{T} \int_0^T \left(At - \frac{1}{2} AT \right)^2 dt \\ &= \frac{1}{12} A^2 T^2. \end{aligned} \quad (\text{S9})$$

Finally, apparent particle brightness B_{app} can be obtained from equations (S6, S8, S9) and (13, 17-19):

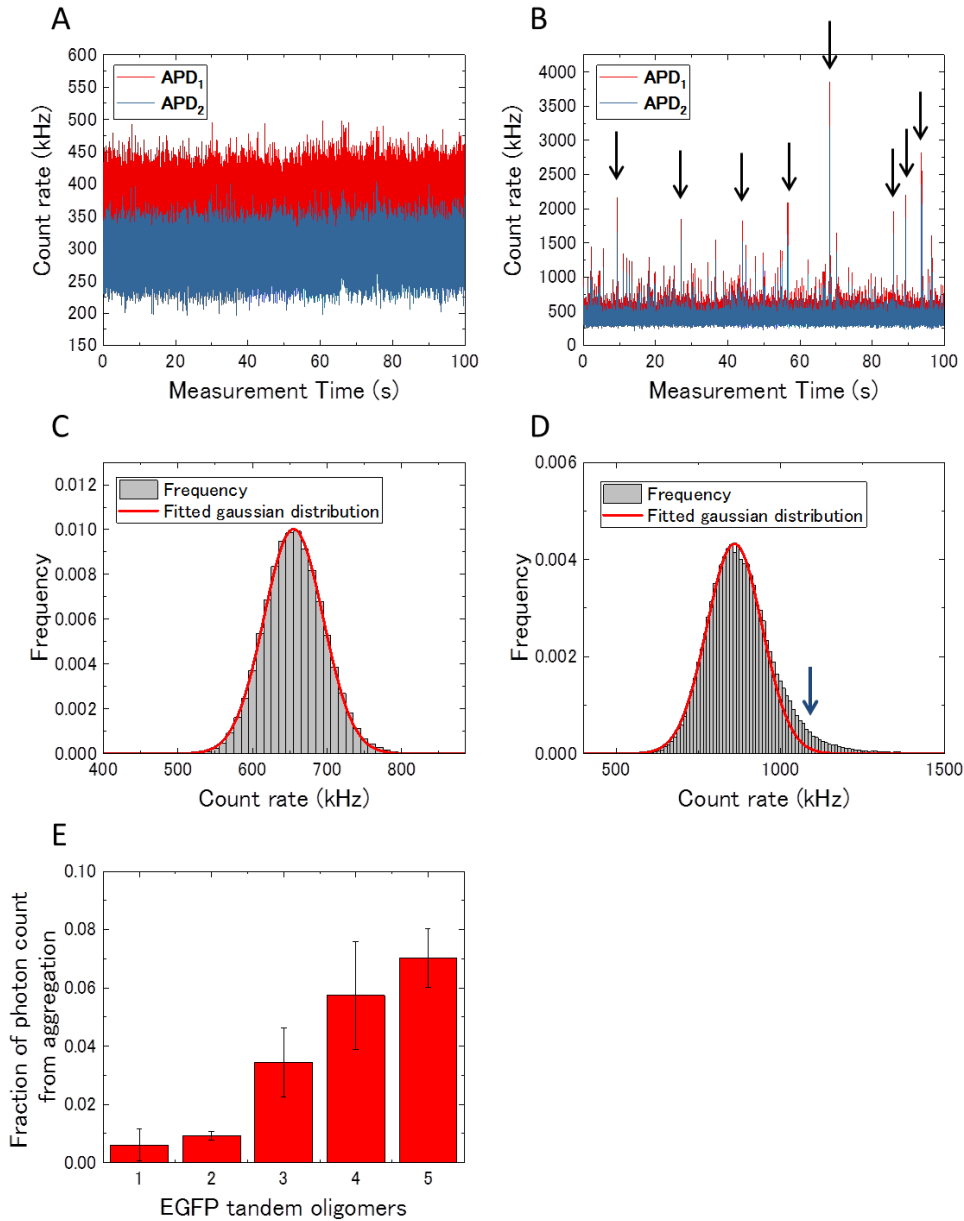
$$B_{app} = \varepsilon + \frac{1}{12} \frac{A^2 T^2}{\langle N(t) \rangle} \varepsilon. \quad (\text{S10})$$

In equation (S10), the second term is always larger than 0 when the slope of the linear component A is not 0:

$$\frac{A^2 T^2}{\langle N(t) \rangle} \varepsilon \geq 0. \quad (\text{S11})$$

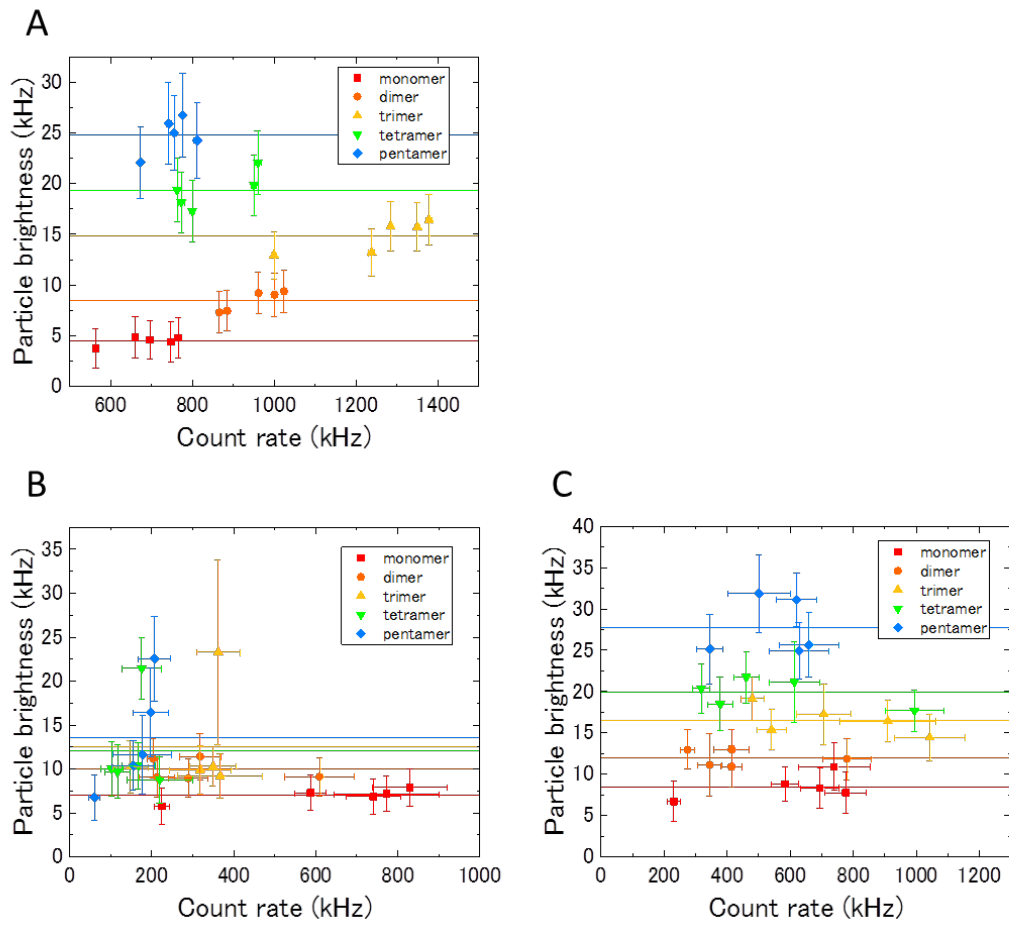
Therefore, the concentration change in measurement time cause overestimation of particle brightness when the linear regression is not performed:

$$B_{app} \geq B = \varepsilon. \quad (\text{S12})$$



Supplementary Figure S2. Aggregation of EGFP tandem oligomers in cell lysate estimated by the distribution of photon counts in FCS.

(A) and (B) show the fluorescence intensity fluctuation in the EGFP monomer lysate and EGFP pentamer lysate, respectively. High-intensity fluorescence burst were occasionally observed (black arrows). Photon count distribution of the EGFP monomer lysate (C) and EGFP pentamer lysate (D). Frequency was normalized to 1. The distributions were fitted to a normal distribution (red line). Rarely formed aggregated EGFP tandem oligomers were occasionally observed (blue arrow). (E) Fraction of photon count from aggregation was estimated by the area outside of the normal distribution.



Supplementary Figure S3. Particle brightness versus count rate plot.

(A) Particle brightness versus count rate of EGFP tandem oligomer in the lysate. (B) Particle brightness versus count rate of EGFP tandem oligomer in the nuclei of living cells. (C) Particle brightness versus count rate of EGFP tandem oligomer in the cytoplasm of living cells. Colored horizontal lines are average for the particle brightness of EGFP tandem oligomers.

Figure 1

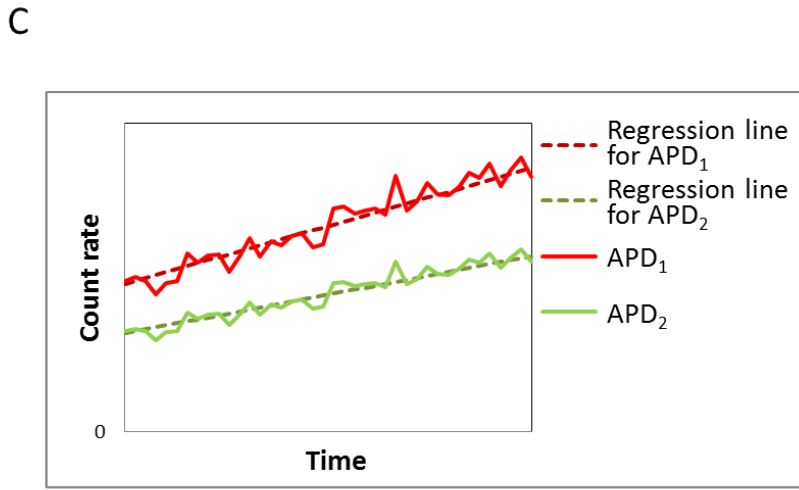
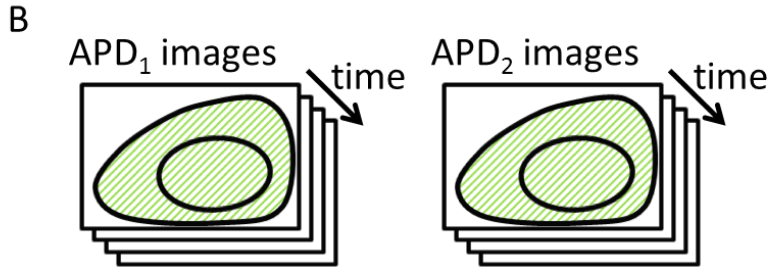
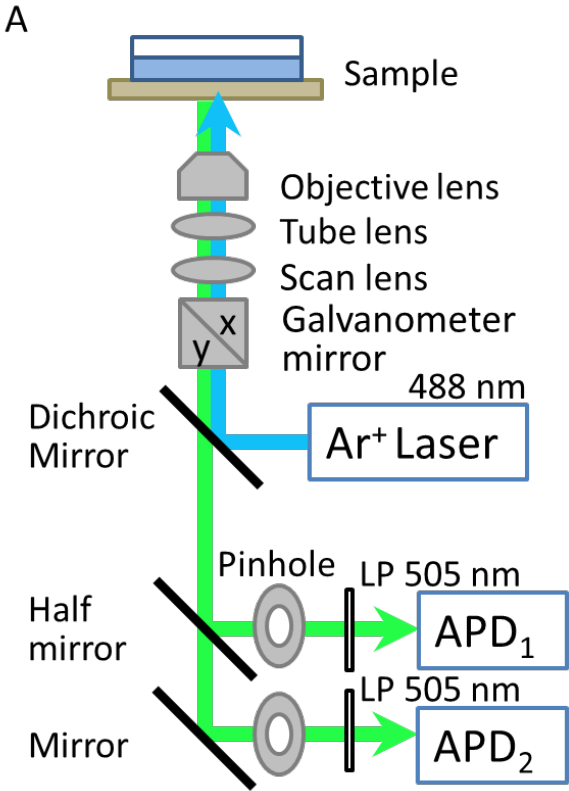


Figure 2

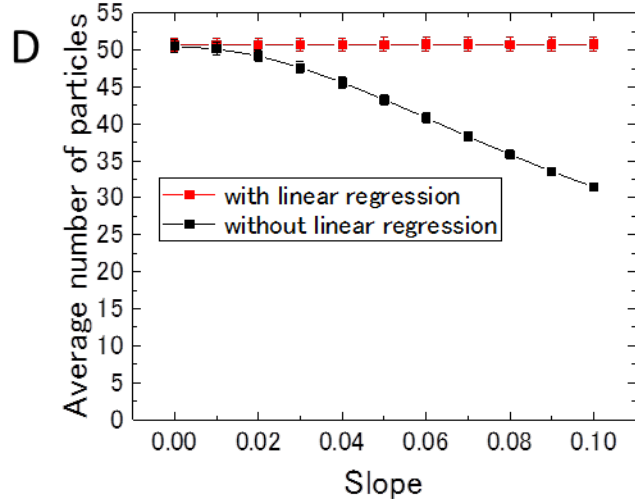
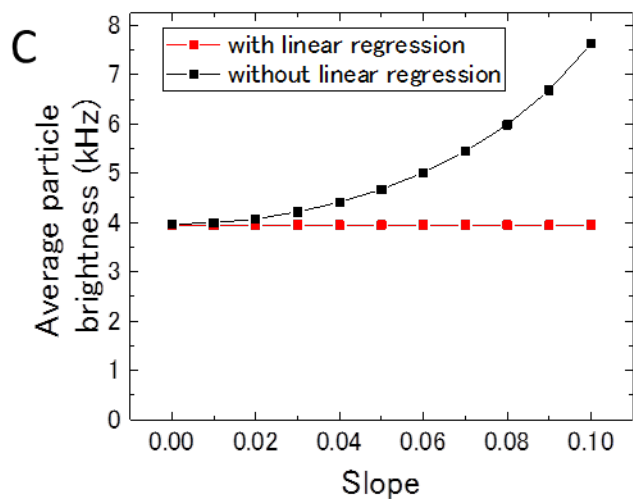
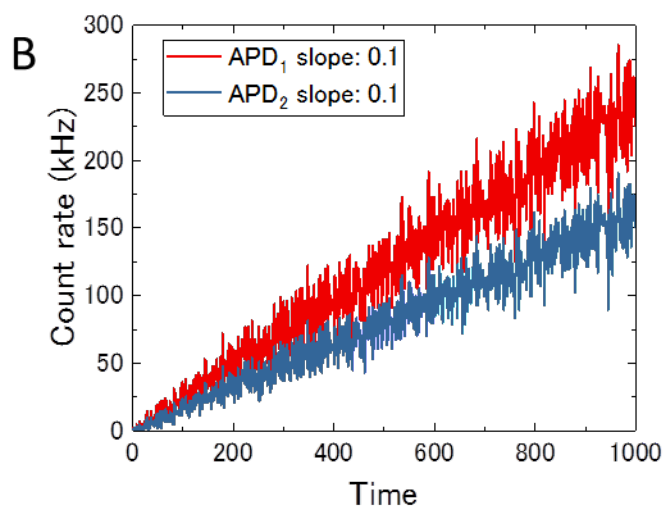
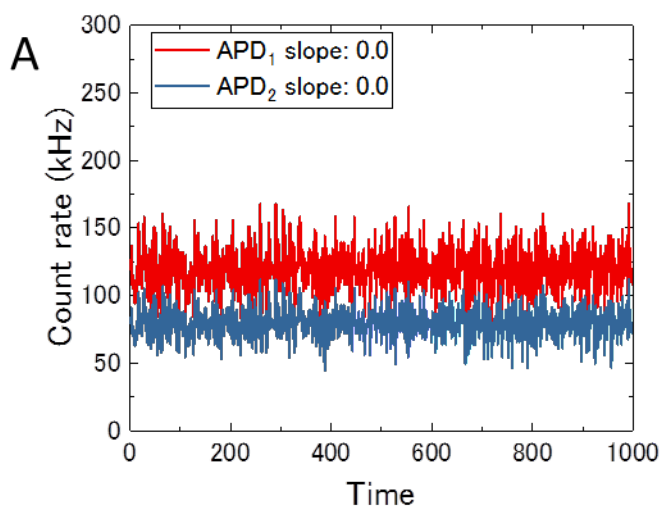


Figure 3

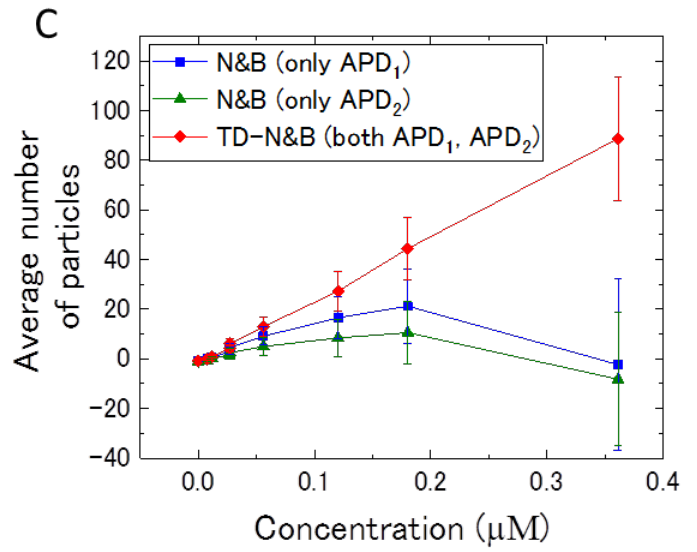
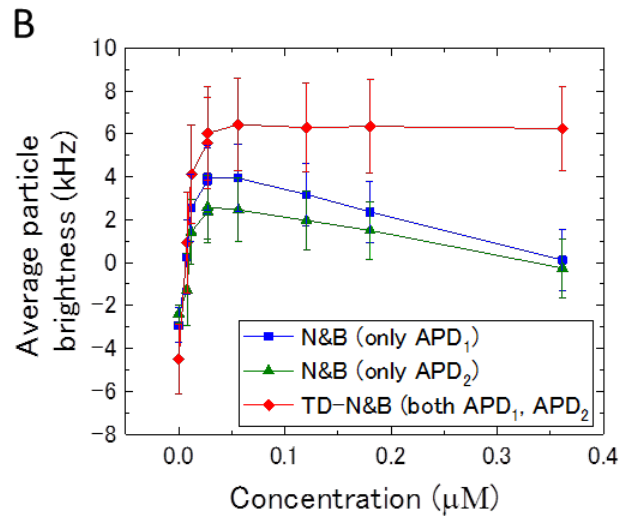
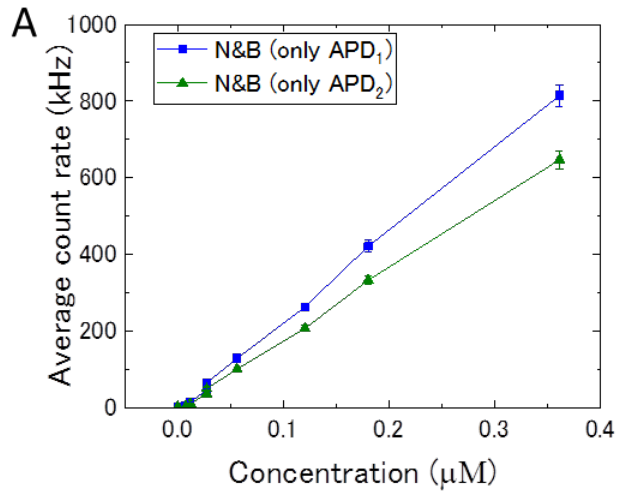
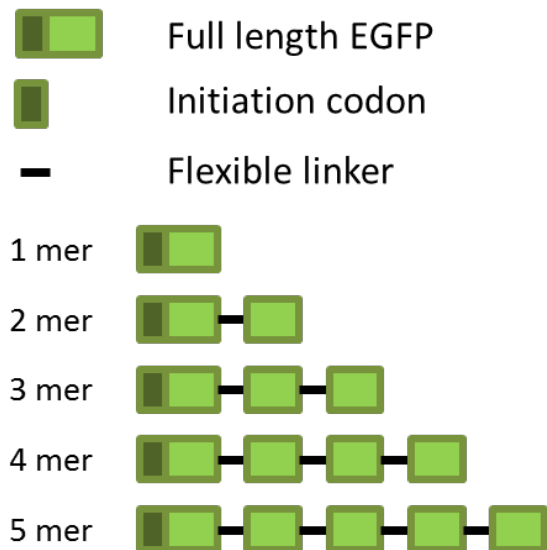
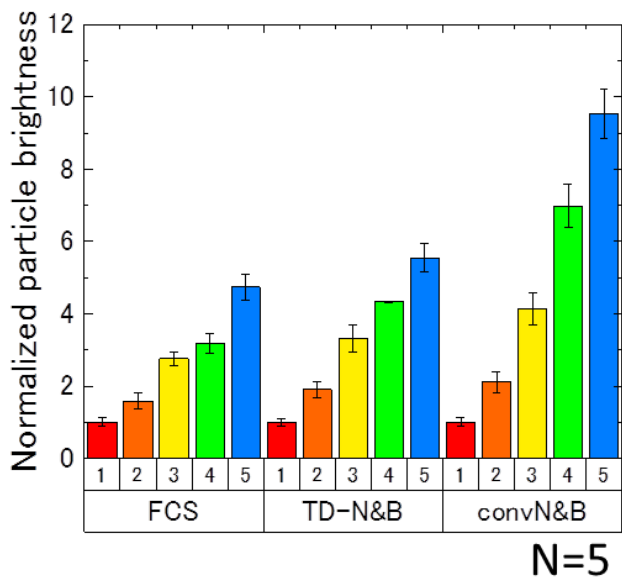


Figure 4

A



B



C

FCS	1	2	3	4	5
1					
2	**				
3	**	**			
4	**	**	*		
5	**	**	**	**	

D

TD-N&B	1	2	3	4	5
1					
2	**				
3	**	**			
4	**	**	**		
5	**	**	**	**	

E

convN&B	1	2	3	4	5
1					
2	**				
3	**	**			
4	**	**	**		
5	**	**	**	**	

F

	FCS/TD-N&B	FCS/convN&B	TD-N&B/convN&B
1	ns	ns	ns
2	*	**	ns
3	**	**	*
4	**	**	**
5	**	**	**

Figure 5

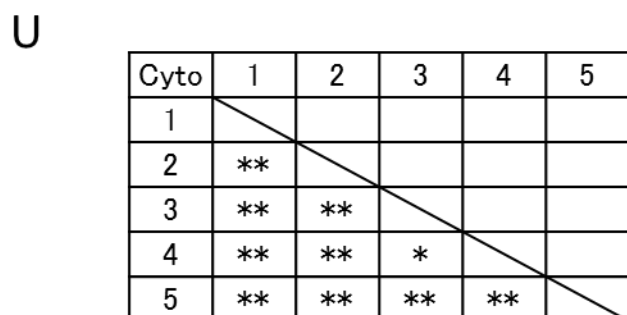
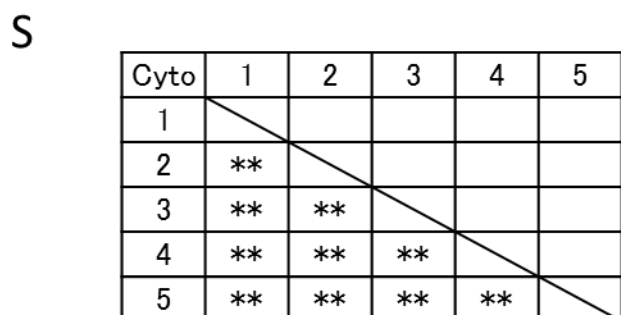
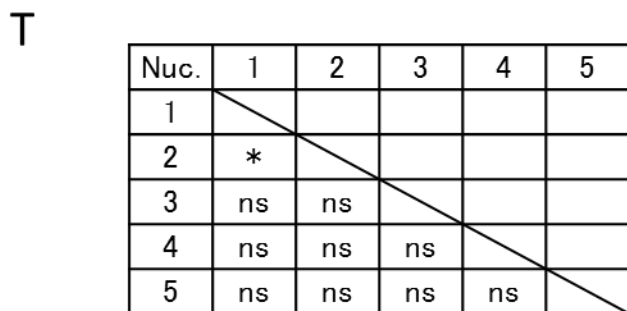
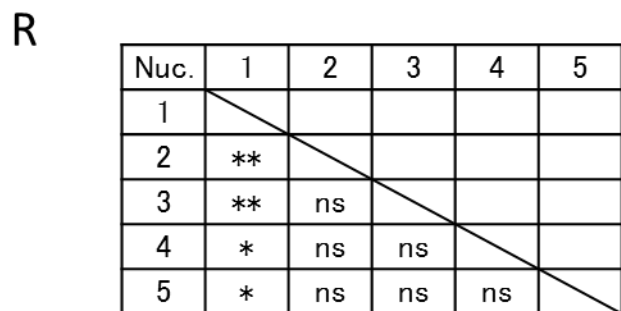
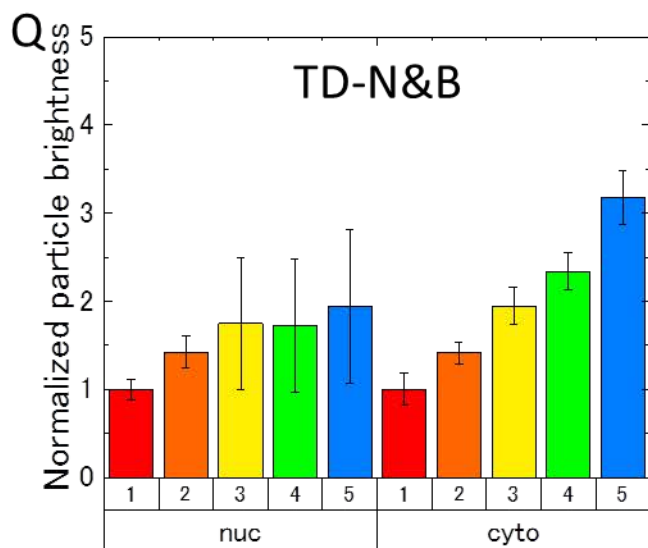
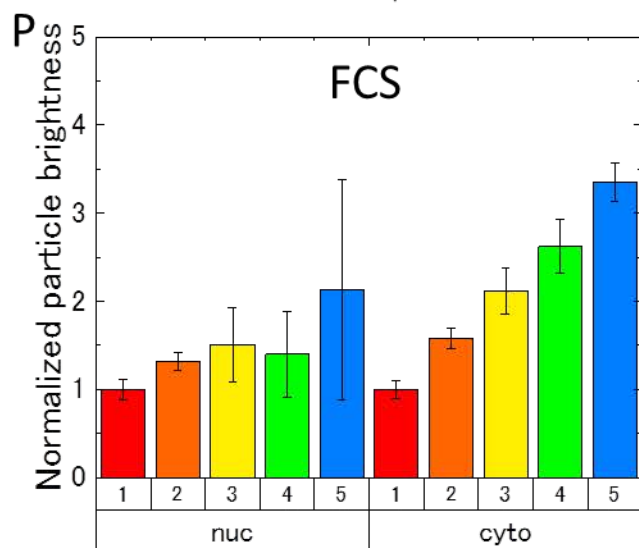
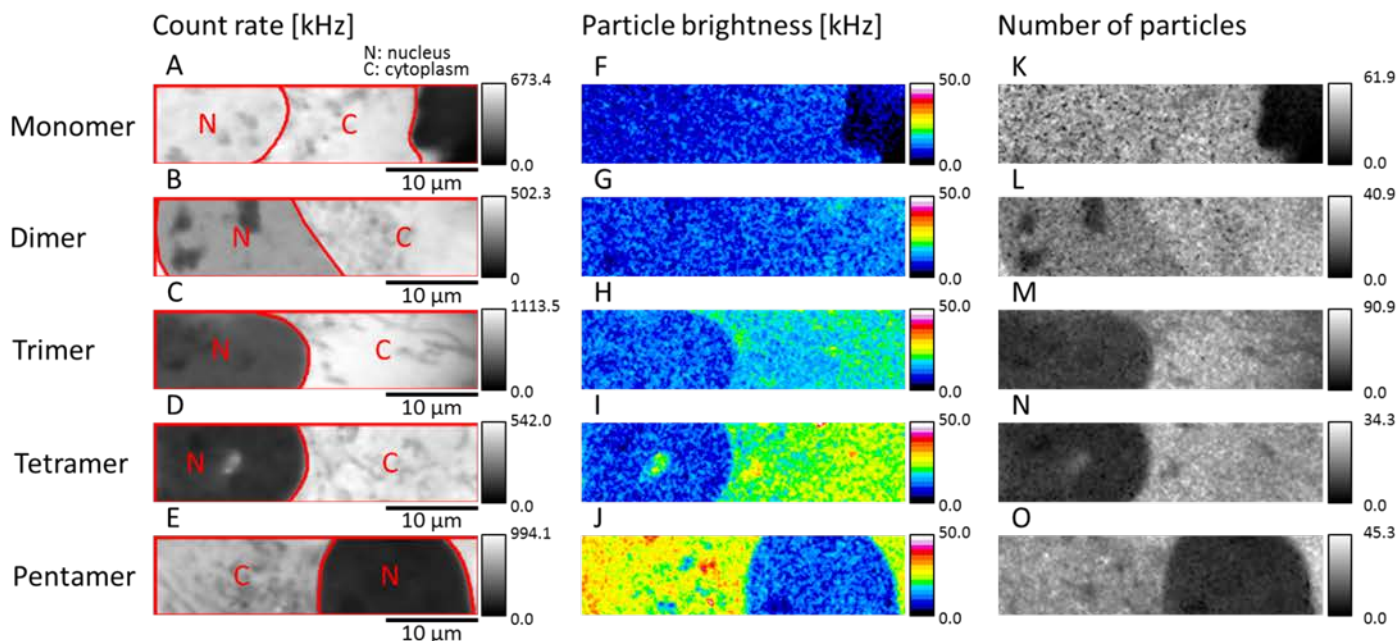


Figure 6

